Supplementary Materials for

PlanetGSD: A Global Dataset of Grain-Size Distributions from Earth, the Moon, and Mars

Jun Zhang[1,2], Yong Li[1*]

[1] Key Laboratory of Mountain Hazards and Engineering Resilience /Institute of Mountain Hazards and Environment, Chinese Academy of Sciences, Chengdu 610213, China

[2] State Key Laboratory of Hydroscience and Engineering; Department of Hydraulic Engineering, Tsinghua University, Beijing 100084, China

Contents of this file

Text S1. Terrestrial Field Sampling and Laboratory Analysis

This section provides the complete instrument specifications, operating parameters, sampling site metadata, and quality control procedures for the combined sieving–laser diffraction protocol applied to all 2,847 field-collected terrestrial samples.

S1.1 Sampling protocol

Terrestrial field samples (n = 2,847) were collected during campaigns conducted between 2015 and 2023 across 18 countries on five continents (Asia, Europe, Africa, North America, Australia). Sampling targeted the upper 10 cm of the surface layer to ensure consistency with the actively weathering zone and to facilitate comparison with orbital remote sensing data. At vegetated sites, surface organic litter was removed prior to sampling.

Sampling strategy by geomorphic setting. The sampling approach was tailored to geomorphic context:

- For relatively homogeneous terrain (plains, grasslands, deserts), systematic grid-based transects with 50–200 m spacing were employed.
- For heterogeneous environments (debris-flow deposits, landslides, moraines), targeted sampling of distinct geomorphic units was applied to capture local variability.

Sample mass and handling. Individual sample mass ranged from 200 g to 2 kg (median 500 g) to ensure sufficient material for combined sieving–laser diffraction analysis and to obtain representative samples of heterogeneous deposits. Samples were immediately sealed in labeled polyethylene bags, and Global Positioning System (GPS) coordinates were recorded (WGS84 datum, decimal degrees). All samples were transported to the laboratory and stored at 4°C prior to analysis (maximum storage duration: 6 months).

S1.2 Laboratory analysis protocol

All field-collected samples (n = 2,847) were processed using a combined sieving–laser diffraction protocol comprising four stages:

Stage 1: Sample preparation. Samples were oven-dried at 104 ± 2°C for 8–12 h until constant mass (weight change <0.1% over successive 2 h intervals). Dried samples were gently disaggregated with a rubber pestle to break up loosely bound aggregates without fracturing individual grains.

Stage 2: Coarse fraction analysis (≥0.25 mm). Dry sieving was performed using a Retsch AS 200 vibrating sieve shaker (amplitude 1.5 mm, frequency 50 Hz, 15 min duration) with a nested

stack of ASTM E11-compliant meshes: 20, 10, 5, 2, 0.5, and 0.25 mm. Mass retained on each sieve was recorded to ±0.01 g.

Stage 3: Fine fraction analysis (<0.25 mm). The fine fraction was analyzed with a Malvern Mastersizer 3000 laser diffractometer (Mie theory, measurement range 0.01–3,500 μm). Sub-samples (0.5–2.0 g) were dispersed in 800 mL deionized water containing 0.05% (w/v) sodium hexametaphosphate and ultrasonicated (40 kHz, 2 min, 30 W). Refractive index settings: 1.55 (real), 0.1 (imaginary). Each sample was measured in triplicate; the median distribution was retained.

Stage 4: Data integration. Sieving mass percentages and laser diffraction volume percentages were merged assuming particle density ρ = 2.65 g/cm^3 (quartz-equivalent) following Konert & Vandenberghe (1997). The combined dataset was binned into the 17 standard size classes listed in Table 1 (main text), following USDA and Wentworth classification schemes. Grain frequency $P(D_i)$ for the i-th size interval was calculated as:

$$P(D_i) = \frac{m(D_i)}{M_{total}} \tag{1}$$

Where $m(D_i)$ is the mass of grains in the i-th size interval and M_{total} is the total sample mass (Yong et al., 2017). Cumulative exceedance percentages were subsequently derived from the frequency distribution. The complete analytical workflow, including quality control checkpoints, is illustrated in Figure S1.

S1.3 Quality control

All laboratory analyses followed standard protocols as specified in BS 1377-2, ASTM D422-63, ASTM D6913-04, and ISO 11277:2009. No additional replicate analyses or certified reference material measurements were performed specifically for this study; measurement uncertainty is therefore not quantitatively assessed. Users should interpret the data with this limitation in mind.

All procedures comply with the cited standards.

S1.4 Literature data screening criteria

Publications employing dry sieving alone or pipette methods without laser diffraction validation were excluded due to incomplete clay fraction characterization or lack of methodological standardization with the combined sieving–laser diffraction protocol adopted as the baseline for this study (BS 1377-2, ASTM D422-63, ASTM D6913-04, ISO 11277:2009). The remaining 43

publications (1,572 samples) all employed methods consistent with this baseline, ensuring cross-study comparability.

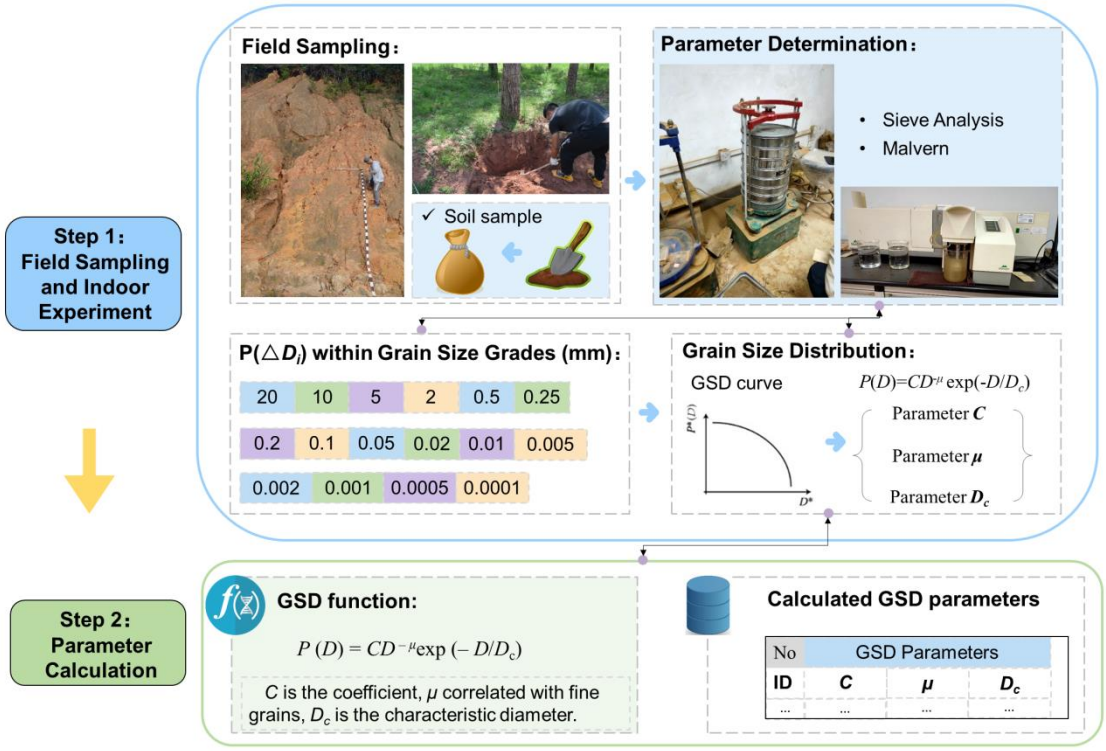

Figure S1. Workflow for terrestrial GSD analysis and UGSD parameterization. (a) Four-stage laboratory protocol: oven-drying, dry sieving (≥0.25 mm), laser diffraction (<0.25 mm), and data integration. (b) Binning into 17 standard size classes (Table 1, main text). (c) UGSD fitting to extract parameters C, μ, D_c, n. (d) Quality control checkpoints: duplicate analysis, certified reference material, and cross-method validation. This workflow was applied to all 2,847 field-collected samples. Median fitting quality across all terrestrial samples: $R^2 = 0.991$.

Table S1. Terrestrial soil sampling sites in Asia

Soil sample	Soil texture	Locations	Specimen number	Brief description	Data sources
APZ	Vegetation covered soils	Apuzu, Liangshan Yi Autonomous Prefecture, SW China	35	Red soil	Sampled by authors
CD	Basin sediment, purple soils	Chengdu, SW China	35	Fluvial deposition	
DF	Debris flow materials	SW China	438	Wide-ranged soils and sediment	
Ord	Grass land	Erdos, NE China	42	Highland	Jin et al.,

	soil				pasture	2011
HN	Tropic soils	Hainan, S China		35	Yellow soils	Sampled by authors
Hor	Grassland soil	Horqin, NE China		65	Dark loessial soil, Kastanozems	
JSR	Jinsha River	Sichuan, SW China		146	Torrid red and purple soils	
JZG	Wind erosion soil	Jiuzhaigou, SW China		47	Loess	
KLM	Cold permafrost and desert soils	Kunlun mountain, NW China		21	At different elevations	Gui, et al., 2010
MDG	Debris flow deposit	Midui Gully	Tibetan Plateau, China	23	At debris flow gully	Sampled by authors
LLR	Moraine	Lulang River		18	On the surface of river bank	
MJ	Riverside surface soils	Minjiang, SW China		825	Yellow brown soils	
MLP	Vegetated and bare slopes	Malipo, S China		570	Red soils	
MSZ	Vegetated covered soils	Mianzhu town, SW China		58	Brown soils	Sampled by authors
TG	Grassland	Tibet, SW China		107	Cold alpine, meadow soil	
TMD	Moraine deposit	Tibet, SW China		38	Moraines and other sediments	
XC	Vegetated covered soils	Xichang, SW China		960	Brown soils	
YM	Brown soil	Yimeng Mountain, E China		37	Vegetated land	Liu et al., 2009
YN	Red soil	Yunnan, SW China		58	Highly, moderately, and weakly weathered "relict" paleosols	Sampled by authors
HM	red yellow soil	Hwangsan-Myun, South Korea		5	on the gentle and low hills in the coastal area	Park, 1987
GM		Gamgok-Myun, South Korea		7		
SBM-m	Brown forest soil	Hinano mountain	Sanyo Buntokuden Memorial, Takamatsu, Kagawa Prefecture, Japan	5	Hinano Mountain and hill	Obara, 2015
SBM-h		Nearby park on the hill		5		
SBM-b		Beside main building		7		
OHU-n	Red yellow soil	Inner court north	Old Hiroshima University Faculty of Science building, Hiroshima,	12	Soils from mountain	
OHU-s		Inner court south		9		

		Japan			
KOY	Paddy soil	Yoshijima park, Kurashiki City, Okayama Prefecture, Japan	8	Soils from mountain and hills	
KWS	Kanto loam soil	Shinonome No. 2 park, Koto Ward, Tokyo, Japan	5		
NTU	Old alluvium soil	Nanyang Technological University in Singapore	32	from slopes of granite and metamorphic rocks	Ghosh, 2019
OMK	Red soil	Omkoi in Thailand	28	Siliceous soil	Jindaluang, 2013
GCS	Aeolian, fluvial, deltaic and marine sediment	Caspian Sea, Iran	35	soils from the Gomishan suburbs	Samiei-Fard, 2021

Table S2. Terrestrial soil sampling sites in North America

Soil sample	Soil texture	Locations	Specimen number	Brief description	Data sources
Nev	Desertification soil	Nevada, USA	120	Desertified soil	Spriggs & Ray-Maitra, 2007
TS	Golf course	USA	24	Topdressing sand	Arya, 2008
CS				Concrete sand	
BS				Bunker sand	
SCS	Sandy coastal plain terrace	Southern California, USA	22	Fine clay soil	Torrent, 1980
MLS	Kalkaska County	Michigan, USA	11	Montcalm loamy sand	Wurman, 1959
MFS	Kent County		7	Montcalm fine sand	
CFS	Calhoun County		7	Coloma fine sand	
WS	Kalkaska County		6	Wallace sand	
MDM	Dredged materials deposit	Somerset County, State of Maryland, USA	7	Acid sulfate soil	Demas, 2004
MTM	Tidal marsh		9		
ALS	Quaternary terraces of the Tallapoosa River	East-Central Alabama, USA	49	Coarse/fine loamy soil	Shaw, 2003
MPS	Beach ridges on the Northern shore of Lake Michigan	Northern Michigan, USA	43	Strand plain soil	Barrett, 2001
CCS	Crosby county	West Texas, USA	55	Sediments of the Blackwater Draw and Ogallala Formations	Hirmas, 2007
HCS	Hudspeth county		6	Underling limestone residuum	
WLS	Northeast Dane County	Wisconsin, USA	13	Soil containing lamellae	Bockheim, 2013
SNC	Western slope of the Sierra Nevada	Western USA	31	Soils on Andesitic	Rasmussen, 2007

	of California			Lahar	
FL	Fine loamy soil	Canada	41	Central Saskatchewan	Amelung, 1999

Table S3. Terrestrial soil sampling sites in Africa

Soil sample	Soil texture	Locations	Specimen number	Brief description	Data sources
Nig	Soils from agricultural landscapes of a derived savanna	Nigerian	15	soil from Ibaadan, Nigerian	Salako, 2006

Table S4. Terrestrial soil sampling sites in Europe

Soil sample	Soil texture	Locations		Specimen number	Brief description	Data sources
GIL	reddish brown soil	Ehwald, Germany		17	in the eastern part of the country, in the state of Saxony-Anhalt	《from soil map volume of Europe》
Kot	dark reddish brown soil	Kottenforst, Germany		23		
Boy	heavy clay	Boyadgiev, Bulgaria		21	Soil collected from agricultural fields	
ALL	sandy loam	Allier	France	12	Soil from hills, plains, and valleys	
CdR	dark brown soil	Cime de Rouyon		5	Soil from Alps	
Cou	yellowish brown soil	Coup d'Alzac		6	Soil from Dordogne Valley	
Lac	reddish brown soil	Lachamp Raphaël		12	Soil from alpine meadow	
MAT	dark brown soil	Mathieu		10		
MOR	dark brown soil	Morozova, Moscow		12	Soil from forested areas	
Dob	dark grey soil	Dobrogostów, Poland		14	Soil from coniferous forests	
MOS	dark grey soil	Grin, Moscow, Russia		20	Soil from the Western Siberian Plain	
Tis	dark greyish brown soil	Crisul Alb, Romania		30	soil from Tisza River Plain	
Kul	brown soil	Kulbäcksliden, Sweden		35	Soil from agricultural areas	

Table S5. Terrestrial soil sampling sites in Australia

Soil sample	Soil texture	Locations	Specimen number	Brief description	Data sources
GOO	sandy loam	Goodwyn, Australia	20	Soil samples from coastal	Minasny, 2007

Text S2. Literature-Derived Terrestrial Samples

S2.1 Literature screening

A total of 43 peer-reviewed publications reporting terrestrial grain-size distribution data were compiled for this study. All selected studies met four inclusion criteria: (i) combined sieving for fractions ≥0.063 mm with laser diffraction or hydrometer analysis for fractions <0.063 mm, consistent with BS 1377-2, ASTM D422-63, ASTM D6913-04, or ISO 11277:2009 standards; (ii) complete size-range cosverage including clay fractions (<2 μm); (iii) cumulative percentages reported in tabular form or in figures of sufficient resolution for accurate digitization; and (iv) geographic coordinates or detailed location descriptions provided.

S2.2 Data extraction

For studies reporting data in tabular form, cumulative grain-size percentages were transcribed directly. For studies reporting data only in graphical format, figures were digitized using WebPlotDigitizer (version 4.5; Rohatgi, 2021). For each figure, at least 10 control points were used to calibrate axes, and data points were extracted at the size classes reported in the original publication. Where studies reported different bin structures than the 17-class framework used in this study, we retained the original size points and applied UGSD fitting (Section 2.4, main text) without interpolation to avoid introducing artifacts.

All extracted data and source citations are provided in Dataset S1.

S2.3 Data sources

The complete list of 43 literature sources is provided in the "Data sources" column of Supplementary Tables S1–S5 and in Dataset S1. Each entry includes the full citation and, where available, the DOI or URL for original publication access.

Text S3. Lunar Sample Data

S3.1 Mission overview and sample sources

The lunar component comprises 379 samples from eight sample-return missions spanning 1969–2024 (Fig. 2; Supplementary Table S6): Apollo 11, 12, 14, 15, 16, and 17 (USA, 1969–1972), Luna 16, 20, and 24 (USSR, 1970–1976), and Chang'e-5 and Chang'e-6 (China, 2020 and 2024). These missions provide geographic coverage of mare basalt plains (Apollo 11, 12, 17; Luna 16, 24; Chang'e-5), basin-margin highlands (Apollo 14, 16), mare–highland contact zones (Apollo 15),

highland terrains (Luna 20), and the lunar farside South Pole-Aitken basin (Chang'e-6).

Grain-size distribution data were compiled exclusively from published literature; no physical lunar samples were processed by the authors. The majority of samples (n = 321, 85%) were digitized from the NASA Lunar Soils Grain Size Catalog (Graf, 1993), a comprehensive compilation of Apollo and Luna grain-size distributions measured between 1969 and 1976 using dry sieving protocols. Additional data were obtained from Heiken et al. (1991) for selected Apollo samples (n = 56), Zhang et al. (2022) for Chang'e-5 sample CE5C0400 (n = 1), and Li et al. (2024) for preliminary Chang'e-6 characterization (n = 1).

S3.2 Sieving protocols

For Apollo and Luna missions, dry sieving was performed using nested sieve stacks with mesh sequences that varied by mission. The standard sieve sizes employed across missions included: 0.1, 0.2, 0.25, 0.5, 1, 2, 5, 10, 20, and 40 mm (Graf, 1993). Sample masses ranged from 1.5 to 3 kg (typical Apollo drive tube samples) to <1 g (some Luna return samples). Sieving was conducted using mechanical sieve shakers with vibration amplitude corresponding to 360 V (manufacturer-specific units) and duration of 20 min per sample (Graf, 1993). Prior to analysis, samples were oven-dried at 104°C for 24 h and gently disaggregated using a mortar and pestle to break up loosely bound aggregates without fracturing individual grains (Heiken et al., 1991). All lunar samples in the database have masses >5 g; therefore, no mass-based filtering is required.

S3.3 Data extraction and harmonization

Cumulative grain-size distributions were extracted from published tables or digitized from figures using WebPlotDigitizer software (version 4.5; Rohatgi, 2020). The number of reported size fractions varies by mission protocol, ranging from 9 (Luna) to 15 (Apollo 15, 17), reflecting differences in sieve mesh sequences employed across programs. Grain sizes span approximately 0.001–10 mm, covering the silt-to-gravel range.

Due to variations in sieve mesh sequences across missions, raw lunar GSD data exhibit heterogeneous bin resolutions. However, the UGSD fitting procedure (Section 2.4.2, main text) operates on cumulative percentages at their original grain-size points without requiring interpolation or re-binning, thereby accommodating these mission-specific protocols while preserving original measurement fidelity. This approach ensures that cross-mission comparability is achieved at the parameterization level rather than through potentially biased interpolation of raw data.

Detailed site descriptions, mission dates, sample types, landing-site coordinates, and original data sources are provided in Supplementary Table S6. The complete lunar dataset is available as Dataset S2.

Table S6. Soil information from the Moon

Soil sample	Soil characters	Lander Coordinates	Landing Date	Specimen number	Sample Return (kg)	Brief description	Data sources
Apollo 11	ranging from sub-micrometer to millimeter scales	Latitude: 0.674° N, Longitude: 23.473° E	20 Jul 1969	21	21.55	southwestern part of Mare Tranquillitatis	Graf, 1993
Apollo 12	ranging from fine dust to coarse detritus	Latitude: 3.013° S, Longitude: 23.422° W	19 Nov 1969	20	34.35	the Mare Cognitum region, southeastern Oceanus Procellarum	
Apollo 14	generally coarser and more poorly sorted	Latitude: 3.646° S, Longitude: 17.472° W	05 Feb 1971	26	42.28	Fra Mauro Highlands	
Apollo 15	generally fine particles	Latitude: 26.132° N, Longitude: 3.633° E	30 Jul 1971	63	77.31	the Hadley-Apennine region at the foot of the Montes Apenninus	
Apollo 16	ranging from sub-micrometer to millimeter scales	Latitude: 8.973° S, Longitude: 15.501° E	20 Apr 1972	5	95.71	the Descartes Highlands region of the lunar nearside	
Apollo 17	submicron dust to centimeter-scale lithic fragments	Latitude: 20.191° N, Longitude: 30.772° E	11 Dec 1972	43	110.52	the Taurus-Littrow Valley	
CE5C0400	average GSD < 10 μm, high maturity and prolonged space weathering	Latitude: 43.058° N, Longitude: 51.916° W	1 Dec 2020	1	/	the Northern Oceanus Procellarum near Mons Rümker	Zhang, 2022
CE-6	Soil grains ranging from <17.6 μm to ~862.4 μm in diameter	41.625° S, 153.978° W	25 Jun, 2024	1	1.935	the South Pole-Aitken basin on the lunar farside	Li, 2024

Source: https://nssdc.gsfc.nasa.gov/planetary/lunar/apolloland.html

Text S4. Martian Image-Based Grain-Size Analysis

This section provides detailed protocols for image selection, grain-size measurement, quality control, and uncertainty assessment for all Martian samples in PlanetGSD 1.0. A summary of the geological context for each landing site is provided in Table S7.

S4.1 Image selection criteria

Images were selected from the PDS archive following established protocols (Fedo et al., 2015; Weitz et al., 2006) to ensure optimal conditions for grain-size measurement:

(i) Known target distance. Target distance was extracted from rover telemetry metadata (ROVER_MOTION_COUNTER or range from laser autofocus), with accuracy of ±5 cm for arm-mounted instruments and ±10 m for mast-mounted cameras. Only images with documented target distances were retained.

(ii) Viewing geometry. Only images with viewing angle <30° from vertical (measured from surface normal) were retained to minimize perspective distortion and grain foreshortening effects. Viewing angle was calculated from camera pointing metadata.

(iii) Illumination conditions. Solar elevation >20° was required to ensure adequate shadow contrast for grain boundary identification. Solar elevation was extracted from image metadata (Solar_Longitude and Local_True_Solar_Time). Images acquired during dust storms or with significant atmospheric haze ($\tau > 1.5$ from Mastcam opacity measurements) were excluded.

A total of 2,160 images meeting these criteria were analyzed to produce the 1,729 grain-size distributions in Dataset S3. The distribution of samples across different geological sub-units at each landing site is detailed in Table S8.

S4.2 Grain-size analysis protocol

Grain-size distributions were measured using semi-automated image-processing software developed by Shi et al. (2021) and Zhao et al. (2023), implemented in Mathematica. The analysis workflow comprises four steps:

Step 1: Image preprocessing. Images were radiometrically calibrated to remove instrumental artifacts (dark current, flat-field response) using PDS-provided calibration files. Contrast was enhanced using adaptive histogram equalization (CLAHE algorithm, tile size 8×8 pixels, clip limit

0.02) to improve grain boundary visibility while avoiding amplification of noise.

Step 2: Grain segmentation. Individual grains were identified using a combination of edge detection (Canny algorithm with Gaussian smoothing, σ = 1.5, threshold hysteresis 0.1/0.3) and marker-controlled watershed segmentation. The software semi-automatically delineates grain boundaries, with manual correction by the analyst for overlapping or poorly defined grains. For each image, 150–500 grains (median 280) were segmented. Only grains with >70% of their boundary visible within the image frame were retained to avoid truncation bias.

Step 3: Size measurement. For each segmented grain, the software calculates the equivalent circular diameter (ECD):

$$D = 2\sqrt{\frac{A}{\pi}} \tag{2}$$

where A is the grain area in pixels. This diameter approximates the intermediate (b-axis) diameter used in terrestrial sieve analysis. Pixel dimensions were converted to millimeters using target distance and instrument focal length from image metadata.

Step 4: Binning and distribution construction. Individual grain measurements were grouped into logarithmic size bins (0.04, 0.1, 0.2, 0.5, 1, 2, 5, 10, 25 mm) and converted to cumulative mass distributions assuming spherical grains of uniform density (ρ = 2.65 g/cm^3, quartz-equivalent). This assumption introduces a potential source of systematic uncertainty when comparing Martian volume-based distributions to terrestrial and lunar mass-based distributions. However, the UGSD fitting procedure operates on normalized cumulative percentages and is robust to such uniform scaling factors (see Section 2.4, main text).

S4.3 Imaging systems and detection limits

Grain-size measurements on Mars utilized a variety of imaging systems with different resolutions and detection capabilities. A detailed summary of these instruments, including their type, pixel scale, working distance, and minimum detectable grain size, is provided in Table 3 of the main manuscript. In brief, the detection limits range from approximately 0.04 mm for arm-mounted imagers (MAHLI, WATSON) to over 0.12 mm for mast-mounted cameras (Mastcam, Mastcam-Z, RMI), with the exact values depending on the instrument and target distance. Users are directed to the main text for the complete specifications and references.

S4.4 Uncertainty assessment

Resolution limitations. The minimum resolvable grain size is instrument-dependent, ranging from ~40 μm for close-range imagers (MAHLI, WATSON) to ~150 μm for mast-mounted cameras (Table S3). Grains smaller than these thresholds cannot be reliably detected and segmented. Consequently, all Martian GSD curves are truncated at the fine end; cumulative percentages for the finest size fraction represent lower bounds rather than absolute values. Users should exercise caution when interpreting fine-fraction statistics (e.g., clay and silt proportions) from Martian samples.

Inter-operator variability. To assess operator-dependent variability in grain boundary delineation, three independent analysts processed identical image sets (n = 30 images spanning all four landing sites) using the same software (Shi et al., 2021; Zhao et al., 2023). For each image, each analyst segmented grains following the standard protocol (S4.2), and UGSD parameters were fitted to the resulting distributions. Differences in grain boundary delineation between operators were quantified using coefficients of variation (CV) for the resulting UGSD parameters:

- μ parameter: mean CV = 6.8% (range 4.2–9.1%)
- D_c parameter: mean CV = 5.7% (range 3.8–8.3%)
- n parameter: mean CV = 7.9% (range 5.1–10.2%)

This variability propagates through the UGSD fitting procedure and is reflected in the parameter confidence intervals reported in Dataset S4. Users should incorporate these uncertainties when conducting comparative analyses sensitive to fine-scale GSD variations.

Systematic biases. The assumption of spherical grains of uniform density (ρ = 2.65 g/cm^3) when converting grain areas to equivalent spherical diameters and subsequently to mass-based cumulative distributions is standard in Martian granulometry studies (Fedo et al., 2015; Weitz et al., 2018). While the UGSD fitting procedure is robust to uniform scaling factors, absolute grain-size values may carry systematic biases relative to sieve-based measurements. Cross-validation with in situ Sieve Analysis (if available) or comparison with terrestrial analogs is recommended for applications requiring absolute accuracy.

S4.5 Data accessibility

Complete source image identifiers (PDS Product IDs) for all 1,729 samples are provided in Dataset S3. For each sample, the following metadata are included: landing site, sub-site, rover, Sol number, instrument, target distance, pixel scale, number of grains segmented, and UGSD fitting

parameters with confidence intervals.

Table S7. Geological context of Martian landing sites

Landing site	Rover	Landing date	Coordinates	Elevation (m)	n samples	Geological age	Main features	Surface processes
Gale Crater	Curiosity	6 Aug 2012	4.59°S, 137.44°E	−4,500	384	Late Noachian–Hesperian	Mt. Sharp sedimentary sequence, paleochannels, alluvial fans	Lacustrine sedimentation, fluvial erosion, aeolian reworking (Grotzinger et al., 2015; Milliken et al., 2010)
Jezero Crater	Perseverance	18 Feb 2021	18.44°N, 77.45°E	−2,530	722	Noachian–Hesperian	Western delta, inlet channel, carbonate outcrops	Deltaic deposition, lake environment, post-depositional erosion (Mangold et al., 2021; Schon et al., 2012)
Gusev Crater	Spirit	4 Jan 2004	14.57°S, 175.47°E	−1,950	366	Noachian (lakes), Hesperian (volcanics)	Ma'adim Vallis outlet, Columbia Hills, volcanic plains	Fluvial flooding, basaltic volcanism, hydrothermal alteration (Cabrol et al., 2003; Ruff et al., 2014)
Meridiani Planu	Opportunity	25-Jan-04	1.95°S, 354.47°E	−1,400	257	Hesperian	Sulfate-rich sandstone,	Evaporite deposition, acidic

m				hematite concretions, aeolian bedforms	groundwater, aeolian transport (Hynek et al., 2017; McLennan et al., 2005)

Note: Coordinates are in IAU Mars 2000 datum. Elevation relative to MOLA areoid. Geological ages follow the Hartmann & Neukum (2001) chronology.

Table S8. Sub-site distribution, sample counts, and geological context for Martian landing sites

Landing site	**Sub-site code**	**Sub-site name**	**Sol range**	***n* samples**	**Dominant lithology / soil type**
Gale Crater	YB	Yellowknife Bay	125–324	36	Ancient lacustrine mudstone; surficial fine to very fine sand
	Gob	Gobabeb	1221–1244	26	Aeolian dune sand (medium to coarse) at Bagnold Dunes edge
	MB	Murray Buttes	1410–1468	34	Eroded lacustrine sandstone; gravelly colluvium
	OB	Ogunquit Beach	2555–2691	62	Bimodal aeolian deposit (fine sand matrix + coarse granules)
	MAG	Mary Anning & Groken	2802–2923	56	Clay-bearing unit; fine-grained (silt/clay) weathering residual
	VRR	Vera Rubin Ridge	2300–2416	96	Hematite-cemented sandstone ridge; mixed coarse debris + aeolian sand
	GT	Glen Torridon	2300–3072	38	Clay-bearing unit; very fine-grained, homogeneous regolith
	GP	Greenheugh Pediment	2691–2734	18	Aeolian sandstone pediment; well-sorted medium sand
	SBU	Sulfate-bearing Unit	2923–3072	6	Erosion-resistant evaporite slopes; coarse, angular debris
	MDI	Mount Desert Island	1650–1660	40	Iron-rich sandstone knob; aeolian sand + local debris
	NBD	Nathan Bridges Dune	1617–1639	28	Active dark dune; extremely well-sorted fine to medium sand
Jezero Crater	ADZ	Adzilili Crater	112–148	22	Small impact crater on delta plain; impact breccia + aeolian sand
	ART	Artuby Ridge	170–200,	90	Carbonate ridge; weathering-dominated coarse debris

			340–343		
	SEI	Seitah	202–286	120	Mg-carbonate/olivine unit; coarse-grained residual mantle
	TFR	Three Forks Region	379–414	72	Delta plain; aeolian-reworked sandy plain
	SKI	Skinner Ridge	477–496	46	Delta front sandstone ridge; coarse talus
	HOG	Hogwallow Flats	501–517	20	Fine-grained delta plain; aeolian-sorted fine sand
	AMA	Amalik	557–581	74	Transitional slope; polymict volcanic-sedimentary mix
	OM	Observation Mountain	593–641	80	Ancient bedrock massif; extremely coarse talus
Gusev Crater	CMA	Columbia Memorial Station	1–36	36	Landing site plain; mixed aeolian sand + local debris
	BC	Bonneville Crater	65–91	52	Young impact crater; ejecta + aeolian infill
	MC	Missoula Crater	93–111	89	Small impact crater; ejecta + aeolian mix
	LC	Lahontan Crater	126–140	81	Moderate-sized crater; composite ejecta/weathering/aeolian mix
	IP	Intercrater Plains	111–126, 140–156	101	Plains between craters; highly homogenized aeolian sand
	CH	Columbia Hills	156–235	92	Ancient bedrock hills; weathering-dominated residual-colluvial
	LL	Larry's Lookout	436–513	60	Ridge-top within Columbia Hills; olivine basalt debris
	HH	Husband Hill	514–705	24	Highest point in Columbia Hills; multi-lithology colluvium
	EID	El Dorado	706–711	67	Light-toned dune field; well-sorted fine sand
	HP	Home Plate	1501–2100	70	Layered volcaniclastic plateau; weakly weathered mixed debris
Meridiani Planum	EAC	Eagle Crater	1–57	40	Small impact crater; sulfate/hematite ejecta + aeolian sand
	FC	Fram Crater	82–90	35	Small crater; well-sorted aeolian sand + hematite spherules

	ENC	Endurance Crater	95–315	53	Medium-sized crater; diverse ejecta/weathering/aeolian mix
	HS	Heat Shield	347–356	46	Anthropogenic impact site; aeolian sand + metallic debris
	PR	Purgatory Ripple	461–484	42	Active aeolian ripple field; well-sorted sand
	VC	Victoria Crater	1292–1622	41	Large complex crater; multi-tiered ejecta + aeolian dunes

Text S5. Fitted Weibull μ Parameters for Grain-Size Distributions

The UGSD parameter μ has been found to satisfy the Weibull distribution (Yong et al., 2017; Zhang et al., 2022, 2023, 2025). Accordingly, Weibull distributions were fitted to the UGSD parameters of terrestrial, lunar, and Martian soils to derive the corresponding μ values (Table S9). These parameters are also provided in Dataset S4 (Sheet 2) in the Figshare repository.

Table S9. Weibull parameters for all sites

Planet	Site	μ_0	k	λ	Dominant process	Geological description
Earth	APZ	0.105	0.114	1.695	Subtropical red soil, vegetated hillslope	Pedogenesis with bioturbation
	XC	0.013	0.023	2.25	Vegetated hillslope, brown soil	
	JSR	0	0.036	3.009	River valley, torrid red and purple soils	Fluvial transport with chemical weathering
	MSZ	0.264	0.246	2.752	Post-earthquake vegetated slope, brown soil	Pedogenesis with mass wasting
	MJ	0.244	0.345	1.014	River bank and floodplain, yellow-brown soil	Fluvial transport and deposition
	CD	0.073	0.195	1.326	Alluvial basin, purple soil	Fluvial deposition
	JZG	0.199	0.283	6.376	Loess-mantled valley, wind-eroded surface	Aeolian deposition and erosion
	NJG	0.001	0.005	0.617	Debris-flow gully, poorly sorted deposit	Gravity-driven transport
	WJG	0	0.020	5.448	Wide-graded gully deposit	Gravity-driven transport with fluvial reworking
	KLM	0.007	0.024	1.303	High-altitude permafrost and desert soil	Cryogenic processes with aeolian erosion
	HN	0.294	0.354	1.354	Tropical lateritic yellow soil	Intense chemical weathering
	YN	0	0.088	1.677	Highly weathered relict paleosol	Chemical weathering (paleo-pedogenesis)

	DF	0.205	0.211	4.726	Debris flow materials, wide-ranged soils	Gravity-driven transport
	MLP	0.040	0.048	4.53	Subtropical vegetated and bare slope, red soil	Pedogenesis with slope erosion
	MDG	0.186	0.147	0.923	Debris flow gully, Tibetan Plateau	Gravity-driven transport
	LLR	0.058	0.049	0.487	Moraine, river bank	Glacial transport
	TMD	0	0.018	1.313	Moraine deposit	Glacial transport
	TG	0	0.134	0.811	Cold alpine meadow soil	Cryogenic processes with biotic influences
	Ord	0.081	0.117	1.144	Grassland, highland pasture	Aeolian erosion with biotic influences
	YM	0.038	0.077	0.564	Vegetated land, brown soil	Biological processes
Moon	Ap 12	0	0.053	2.076	Oceanus Procellarum mare basalt regolith	Impact comminution
	Ap 14	0	0.066	2.050	Fra Mauro highland ejecta blanket	Impact comminution with ejecta mixing
	Ap 15	0	0.067	2.113	Hadley-Apennine mare – highland boundary regolith	Impact comminution
	Ap 16	0.028	0.053	4.482	Descartes highland, multiple ejecta blankets	Impact comminution with multi-source mixing
	Ap 17	0.005	0.077	1.834	Taurus-Littrow valley, mare – highland contact	Impact comminution
	Lu 24	0	0.058	1.834	Mare Crisium basaltic regolith	
Mars	Gob	0.583	0.673	1.011	Aeolian, wind-formed ripples	Aeolian sorting
	MB	0.787	0.909	2.666	Eroded lacustrine sandstone	Lacustrine deposition with aeolian erosion
	MAG	0.839	1.022	2.018	Clay-rich laminated mudstone	Lacustrine processes with chemical weathering
	VRR	0.777	0.804	2.503	Hematite-bearing ridge, erosional	Chemical weathering with aeolian erosion
	MAA	3.142	3.180	5.636	Clay-rich laminated mudstone/siltstone	Hydraulic sorting with chemical weathering
	ADZ	1.026	1.100	2.159	Delta plain, coarse sand/granules	Deltaic deposition
	ART	0.943	0.931	3.003	Weathering-dominated, coarse-grained	Chemical weathering
	SEI	0.712	0.714	1.657	Coarse sand to granules	Aeolian erosion
	BC	0.521	0.729	2.145	Coarse sand to gravel	Aeolian erosion
	CH	1.179	1.279	2.829	Rock outcrops, colluvium, aeolian sand	Mass wasting with aeolian erosion
	LL	0.218	0.367	1.260	Columbia Hills, olivine basalt,	Weakly altered volcanic

				weak weathering	bedrock
HP	0.161	0.433	2.157	Mixed volcanic-sedimentary, weak weathering	Weakly altered volcanic bedrock
EAC	2.654	2.382	1.219	Impact-excavated and aeolian	Impact gardening with aeolian erosion
FC	0.110	0.909	2.666	Well-sorted aeolian and impact ejecta	Aeolian erosion
ENC	0.444	0.673	1.745	Impact ejecta, weathering, and aeolian	Mixed processes
HS	0	0.477	3.029	Aeolian sand dominant	Aeolian erosion

Note: Site-level Weibull parameters are derived from fitting three-parameter Weibull distributions to the μ-value populations at each sampling location. These parameters enable stochastic generation of μ-fields for numerical simulations (see Code S1).

Text S6. Data Analysis Codes and Computational Details

S6.1 Software environment

All data processing and statistical analysis were performed using Python 3.9 with the following packages: NumPy 1.23, SciPy 1.9, and Matplotlib 3.6. All codes are openly available in the PlanetGSD 1.0 repository at Figshare (https://doi.org/10.6084/m9.figshare.31569616) and as supplementary files accompanying this paper.

S6.2 Code descriptions

Code S1: UGSD Parameterization

For each sample, the cumulative GSD curve $P(>D)$ is fitted to the UGSD function (Eq. 1 in main text) using nonlinear least-squares optimization (scipy.optimize.curve_fit) to extract four parameters: C, μ, D_c, and n. Initial parameter guesses are set as $C = 80$, $\mu = 0.5$, $D_c = 10$, and $n = 0.5$. Goodness-of-fit is quantified by R^2. Code S1 accepts input as Excel files (columns: grain size / mm, cumulative percentage / %) and outputs a table of fitted parameters.

Code S2: Weibull Distribution Fitting

At each site, the population of μ values is fitted to the three-parameter Weibull distribution (Eq. 3) using maximum likelihood estimation (scipy.stats.weibull_min.fit). The shape parameter k, scale parameter λ, and location parameter μ_0 are extracted. Code S2 generates diagnostic plots including probability density functions and Q–Q plots for fit validation.

Code S3: Stochastic Granular Field Generation

To construct spatially continuous μ-fields, Code S3 implements the three-step Monte Carlo

workflow of Zhang et al. (2022): (i) generate an ensemble of N random μ values by sampling from the fitted Weibull distribution; (ii) assign values to a DEM-registered grid via inverse-distance-weighted (IDW) interpolation (power = 2); (iii) export the μ-field as GeoTIFF for visualization in GIS software. Users can specify DEM resolution, interpolation radius, and the number of Monte Carlo realizations.

S6.3 Reproducibility

All codes are provided as Jupyter notebooks with example datasets and detailed documentation. Users can reproduce all figures and tables in this paper by running the notebooks sequentially.

Table S10. Computational performance of data analysis codes (tested on Intel i7-10700 CPU with 32 GB RAM)

Code	Task	Execution Time
S1	UGSD fitting	~0.5 s per sample
S2	Weibull parameterization	~2 s per site
S3	μ-field generation	~30 s per 1 km^2